Correction for X-Ray Scatter and Detector Crosstalk in Dark-Field Radiography

Theresa Urban[ID], Wolfgang Noichl[ID], Klaus Juergen Engel, Thomas Koehler[ID], and Franz Pfeiffer[ID]

Abstract—**Dark-field radiography, a new X-ray imaging method, has recently been applied to human chest imaging for the first time. It employs conventional X-ray devices in combination with a Talbot-Lau interferometer with a large field of view, providing both attenuation and dark-field radiographs. It is well known that sample scatter creates artifacts in both modalities. Here, we demonstrate that also X-ray scatter generated by the interferometer as well as detector crosstalk create artifacts in the dark-field radiographs, in addition to the expected loss of spatial resolution.**

We propose deconvolution-based correction methods for the induced artifacts. The kernel for detector crosstalk is measured and fitted to a model, while the kernel for scatter from the analyzer grating is calculated by a Monte-Carlo simulation. To correct for scatter from the sample, we adapt an algorithm used for scatter correction in conventional radiography. We validate the obtained corrections with a water phantom. Finally, we show the impact of detector crosstalk, scatter from the analyzer grating and scatter from the sample and their successful correction on dark-field images of a human thorax.

Index Terms—**Image enhancement/restoration (noise and artifact reduction), X-ray imaging and computed tomography.**

Theresa Urban was with the Chair of Biomedical Physics, Department of Physics, School of Natural Sciences, Technical University of Munich, 85748 Garching, Germany, also with the Munich Institute for Biomedical Engineering, Technical University of Munich, 85748 Garching, Germany, and also with the Department of Diagnostic and Interventional Radiology, School of Medicine and Klinikum rechts der Isar, Technical University of Munich, 85748 Munich, Germany. She is now with the Department of Mechanical Engineering, University College London, WC1E 7JE London, U.K., and also with the European Synchrotron Radiation Facility, 38000 Grenoble, France (e-mail: theresa.urban@tum.de).

Wolfgang Noichl is with the Chair of Biomedical Physics, Department of Physics, School of Natural Sciences, Technical University of Munich, 85748 Garching, Germany, and also with the Munich Institute for Biomedical Engineering, Technical University of Munich, 85748 Garching, Germany (e-mail: wolfgang.noichl@tum.de).

Klaus Juergen Engel is with Philips Innovation and Strategy, 5656 Eindhoven, The Netherlands (e-mail: klaus.j.engel@philips.com).

Thomas Koehler is with Philips Innovative Technologies, 22335 Hamburg, Germany, and also with the Institute for Advanced Study, Technical University of Munich, 85748 Garching, Germany (e-mail: thomas.koehler@philips.com).

Franz Pfeiffer is with the Chair of Biomedical Physics, Department of Physics, School of Natural Sciences, Technical University of Munich, 85748 Garching, Germany, also with the Munich Institute for Biomedical Engineering, Technical University of Munich, 85748 Garching, Germany, also with the Department of Diagnostic and Interventional Radiology, School of Medicine and Klinikum rechts der Isar, Technical University of Munich, 85748 Munich, Germany, and also with the Institute for Advanced Study, Technical University of Munich, 85748 Garching, Germany (e-mail: franz.pfeiffer@tum.de).

Digital Object Identifier 10.1109/TMI.2024.3374974

I. Introduction

DARK-FIELD radiography [1], [2] is a new imaging method that can visualize the micro-structural properties of the investigated object, such as the lung's alveolar structure. For chest imaging, it has just recently been translated to clinical stage and its diagnostic value is currently investigated with a clinical prototype [3]. Initial results from currently ongoing clinical studies showed that dark-field chest radiographs allow the detection and quantification of pulmonary emphysema [3], [4] and the assessment of Covid-19 pneumonia [5]. Among qualitative evaluations by radiologists [3], [5], also a quantitative analysis of the obtained dark-field signal [4], [6] is of great interest, as a quantitative analysis is potentially less work-intensive and yields objective results.

The dark-field signal originates from spatial fluctuations of the wavefront due to unresolved micro-structures in the sample [7]. These spatial fluctuations are induced by coherent ultra-small-angle scattering at inhomogeneities in the sample's electron density, i.e. material interfaces, which are too fine and numerous to be resolved individually. The length scale of material interfaces the system is sensitive to depends on system parameters and is typically in the micrometer range [8]. The dark-field signal is the stronger the more of these microscopic material interfaces the beam passes through [9]. Such interfaces are present in porous structures such as foam, in powders, in fibrous structures such as wood, or, in our case, in the alveolar structure of the lung. Homogeneous materials, such as water or soft tissue, do not generate any ultra-small-angle scattering.

The corresponding angles are so small that the deviation from the original beam position at the detector location is typically below the detector resolution. Therefore, the dark-field signal cannot be measured with conventional radiography systems. Instead, the dark-field signal is measured as the loss
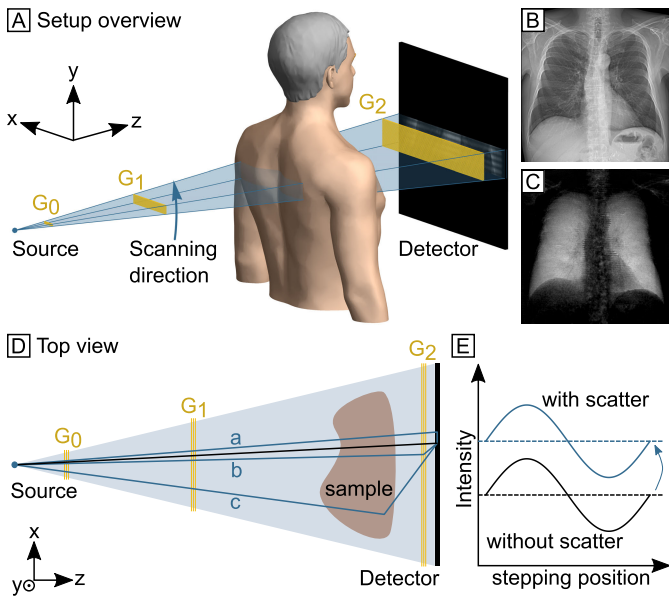
Fig. 1. Overview and effect of scatter and crosstalk in grating-based dark-field imaging. (A) A Talbot-Lau interferometer formed by source grating G_0, phase grating G_1, and analyzer grating G_2 creates an interference pattern with moiré fringes on top of the radiograph. Analysis of a series of exposures with different fringe phase allows to reconstruct an attenuation-based radiograph (B) and a dark-field radiograph (C). (D), Schematic top view of the prototype scanner. The black line depicts the path of an exemplary unscattered photon, whereas blue lines depict exemplary paths of photons contributing to an intensity offset in the same position as the unscattered photon. The three main contributions of this offset are detector crosstalk (path a), scatter from the analyzer grating G_2 (path b) and scatter from the sample (path c). (E), Scatter and crosstalk adds an offset to the stepping curve. Since both attenuation and dark-field signals depend on the mean of the stepping curve, scatter and crosstalk lead to artifacts in the respective images.

of contrast of an interference pattern, which is generated by a Talbot-Lau interferometer formed by three gratings G_0, G_1, and G_2 in the beam path [10], shown in Fig. 1A. The periodic phase shift due to the phase grating G_1 leads to a periodic intensity pattern in certain distances from the grating [11]. This pattern changes with the sample in the beam path. Attenuation leads to a reduction of the mean intensity of this pattern, whereas the term "dark-field signal" is assigned to a reduced contrast, called visibility, of the pattern.

Since the intensity pattern is too fine to be directly resolved with a conventional flat-panel detector, an analyzer grating G_2 with a matching period is placed directly in front of the detector. For conventional clinical sources, an additional source grating G_0 is used to convert the large incoherent source into many small line sources, each with sufficient spatial coherence for interferometry. By a thoughtful choice of the grating parameters, each small line source generates a congruent pattern at the analyzer grating. By taking multiple exposures with varying relative positions of analyzer grating and intensity pattern, a so-called stepping curve is obtained at each pixel, from which the attenuation and dark-field signal can be extracted.

The measured stepping curve is influenced by various other processes besides attenuation and ultra-small-angle scattering which lead to artifacts in the obtained images. Some of these effects are due to interactions of photons with matter, where

the photon still reaches the detector but at a different location than if it did not undergo any interaction (Fig. 1D). These effects include scattering and fluorescence of X-rays in the setup, in particular in the analyzer grating G_2, and optical crosstalk after scintillation in the detector. Furthermore, these effects also include photons reaching the detector after incoherent scattering in the sample as well as coherent scattering in the sample, with angles larger than those corresponding to the dark-field signal. Note that the sample's coherent ultra-small-angle scattering is due to microscopic material interfaces and generates the dark-field signal. Coherent scattering at larger angles – e.g. corresponding to those used in small-angle X-ray scattering experiments [12] – is due to nanometer scale arrangement of atoms and molecules within the volume of materials. It is therefore an unwanted effect in the application of dark-field imaging for the differentiation of different types of tissue. Scatter created upstream of the sample can be neglected, since only photons that actually reach the detector cause artifacts.

Unlike primary radiation, the detector signal generated by scatter or crosstalk barely depends on the relative position of analyzer grating and intensity pattern. Thus, scatter and crosstalk lead to an approximately constant offset on the whole stepping curve (Fig. 1E). The increased mean value of the stepping curve leads to artifacts in the attenuation image that are well known from conventional radiography. The visibility of the stepping curve depends on the mean intensity as well. Therefore, scatter and crosstalk also cause artifacts in the dark-field radiograph which impair image appearance for qualitative analysis and prevent a quantitative analysis of the dark-field signal.

The effect of scatter from the sample in grating-based imaging has previously been studied in [13] for smaller setups in the context of mammography. In the current clinical setup for chest imaging, the effect of sample scatter is more prominent due to the larger exposed volume, the higher photon energy, and a higher total attenuation of the sample. Scatter from the analyzer grating was simulated by Vignero et al. [14], but only its effect on the setup's reference visibility was investigated. To the best of our knowledge, the effect of neither detector crosstalk nor scatter from the analyzer grating in dark-field radiographs have been investigated before.

In this work, we propose deconvolution-based methods to correct for scatter and crosstalk in dark-field and attenuation images via finding the respective scattering kernels. Furthermore, we validate the corrections with a water phantom. Finally, we demonstrate the effect of detector crosstalk, scatter from the analyzer grating and scatter from the sample and their correction on dark-field images of a patient from the current clinical study.

II. THEORY

Dark-field radiography measures the intensity I in a pixel while sampling it with the reference pattern in exposures j. This procedure is performed once for reference without a sample and once with a sample. The measured intensities can be modelled as

$$I_j^r = t_j^r(1 + v_j^r \cos(\varphi_j^r)) \tag{1}$$

for the reference scan and

$$I_j = t_j^r t (1 + v_j^r v \cos(\varphi_j^r + \varphi)) \tag{2}$$

for the sample scan [15], with reference intensity t_j^r, reference visibility v_j^r and reference phase φ_j^r, and sample properties transmission t, relative visibility reduction v and differential phase shift φ. These values are obtained with a least squares fit of the reference and sample scans [15]. The attenuation A and dark-field signal D are then calculated via

$$A = -\ln(t) \quad \text{and} \tag{3}$$
$$D = -\ln(v). \tag{4}$$

We did not further evaluate the phase term φ, because the phase image is so far not used for clinical evaluation.

The scatter intensity generally depends on the exposed volume and the gratings, and detector crosstalk depends on detector illumination. However, to get an approximate estimation of the impact of scatter on dark-field and attenuation images, we consider a simplified case, where scatter is uniform enough so that the scatter intensity does not depend on the exposure index j. Further, we assume that reference intensity t^r and visibility v^r are also independent of exposure index j.

Scatter by the gratings and detector crosstalk occurs in both the reference and the sample scan. The measured intensities I_j then include the primary intensities and an additive scatter and crosstalk intensity I_s. This leads to

$$I_j^r = t^r (1 + v^r \cos(\varphi_j^r)) + I_s^r \tag{5}$$

for the reference scan and

$$I_j = t^r t (1 + v^r v \cos(\varphi_j^r + \varphi)) + I_s \tag{6}$$

for the sample scan. Even in this simplified case, I_s cannot be included as a variable in the least squares fit. For a correction of the ensuing artifacts, it is rather necessary to eliminate the influence of detector crosstalk and scatter from the measurements before the final signal retrieval.

To estimate the impact of scatter and crosstalk when it is ignored in the phase retrieval, equation (5) can be factorized to show the scatter-affected reference intensity $t^{r\prime}$ and reference visibility $v^{r\prime}$, which are obtained when the measured intensities from the reference scan (equation (5)) are fitted with the model in equation (1):

$$I_j^r = t^{r\prime} (1 + v^{r\prime} \cos(\varphi_j^r + \varphi)) \tag{7}$$

with

$$t^{r\prime} = t^r (1 + s^r) \quad \text{and} \tag{8}$$
$$v^{r\prime} = v^r (1 + s^r)^{-1}, \tag{9}$$

where $s^r = I_s^r / t^r$ is the ratio of scatter to primary intensity in the reference scan. These scatter-affected reference values are further used to obtain scatter-affected sample transmission t' and relative visibility reduction v' from the measured intensities in the sample scan, by fitting the measured intensity (equation (6)) using equation (2):

$$I_j = t^{r\prime} t' (1 + v^{r\prime} v' \cos(\varphi_j^r + \varphi)) \tag{10}$$

with

$$t' = t \frac{1+s}{1+s^r} \tag{11}$$

and

$$v' = v \frac{1+s^r}{1+s}, \tag{12}$$

where $s = I_s / t^r t$ is the ratio of scatter to primary intensity in the sample scan.

Note that the phase image φ is not affected by scatter or crosstalk, because, at least in the simplified case here, these only add an offset, but do not change the phase of the measured stepping curve.

We find that scatter and crosstalk lead to an offset S in the corresponding attenuation and dark-field images:

$$A' = -\ln(t') = -\ln(t) - \ln\left(\frac{1+s}{1+s^r}\right) = A - S \tag{13}$$

and

$$D' = -\ln(v') = -\ln(v) - \ln\left(\frac{1+s^r}{1+s}\right) = D + S, \tag{14}$$

where

$$S := \ln\left(\frac{1+s}{1+s^r}\right). \tag{15}$$

The absolute offset in the dark-field signal is the same as for the attenuation signal, albeit with an opposite sign. Since in all practical cases, $s > s^r$ and $S > 0$, the attenuation is underestimated while the dark-field signal is overestimated.

III. METHODS

The following sections show a deconvolution-based approach to eliminate the effects of scatter and crosstalk via finding their respective scatter kernels. Quantitative values are setup-specific, as they depend on hardware components such as detector and gratings, the distances between objects, and the X-ray spectrum. However, the general approach to obtain these corrections can be applied to any grating-based dark-field radiography setup.

A. The Setup

We use the clinical prototype for dark-field chest radiography featuring an oblong active grating area and a fringe scanning acquisition scheme described in [3] and [6]. The setup parameters are listed in Table I. The gratings are oriented with the lamellae in horizontal direction. All gratings are bent cylindrically with their distance from the source as bending radius, to ensure their correct alignment with respect to the beam path also in outer parts of the grating area [16]. Since the production of a grating large enough to cover the whole field of view is currently not possible, we use a scanning acquisition mode [17], [18]. The active area on the detector is about 6.5 cm × 42 cm, and the analyzer grating is stitched from 6 smaller tiles of 6.5 cm × 7 cm each. By slightly detuning the interferometer, moiré fringes are generated in the detector plane, meaning that different interferometer positions relative to a pixel result in different relative positions of analyzer

	G_0	G_1	G_2
distance from source (cm)	30	102	241
period (μm)	7.7	10.1	14.8
height (μm)	250	9.2	250
material	Au	Au	Au
substrate height (μm)	1000	200	1000
substrate material	graphite	glass	graphite
number of tiles	1	1	6

grating and intensity pattern. Thus, a stepping curve can be obtained for each pixel by taking multiple exposures while scanning the interferometer over it. Typically, one full scan consists of 195 exposures, each applied on an area collimated by the slot, resulting in 24 exposures per pixel. See [15] for more details on image reconstruction.

The tube (MRC 200 0508 ROT-GS 1003; Philips Medical Systems) is operated with large focal spot (0.8 as per IEC 60336) and 70 kV tube voltage at $30 \, s^{-1}$ pulse rate while the interferometer is scanned upwards, leading to 195 images per acquisition. The detector (PIXIUM 4343 F4; Trixell) is placed at a distance of 244 cm from the source and features a 600 μm CsI scintillator layer. It is operated with 3×3 binning, resulting in a pixel size of 444 μm $\times$ 444 μm.

B. Detector Crosstalk

In the scope of this paper, the term detector crosstalk is used for all processes that lead to a measured intensity remote from the incident photon, mainly due to the spread of optical photons originating from scintillation [19]. This well-known effect is characterized by a point spread function, leading to a loss of spatial resolution in the recorded exposures and consequently also in the reconstructed attenuation and dark-field images. However, this effect also decreases the measured contrast of the stepping curve wherever the phase of the moiré fringes in pixels in close vicinity differs. This causes a spurious, crosstalk-induced dark-field signal the same way X-ray scatter does.

Depending on the attenuation of the sample, the detector is exposed with varying intensity. Equation (15) shows that the resulting signal S depends on the scatter-to-primary ratio. The worst detector crosstalk impact is expected for image areas of low primary intensity that are close to edges of attenuation, being contaminated by detector crosstalk from closeby areas of high intensity.

The crosstalk intensity I_s can be calculated by a convolution of incident intensity I with a crosstalk kernel k [20]:

$$I_s = I * k. \tag{16}$$

To model the crosstalk kernel k, we assume that optical photons are isotropically scattered with a model according to a 2D-Beer-Lambert decay, expressed as

$$k(r) = \begin{cases} \beta e^{-\alpha r}/r^2 & r > 0 \\ 0 & r = 0, \end{cases} \tag{17}$$

where r denotes the distance from the point of impact of the incident photon. The parameters α and β describe the radial linear attenuation coefficient of the scattered photons and the

overall probability of scattering in the detector, respectively. Photons scattered within one pixel ($r = 0$) are counted as primary intensity.

C. Scatter From the Analyzer Grating

Scatter from the interferometer mainly consists of X-ray photons scattered at the analyzer grating located between sample and detector. The analyzer grating acts both as an anti-scatter grid for all scatter happening upstream as well as a scatter source itself. This includes photons scattered via coherent or incoherent scattering at the substrate, the photoresist, or the grating lamellae, as well as fluorescence photons.

The expected kernel has a complex shape due to the microscopic structure of the grating. For lack of a simple analytic model, we conducted Monte-Carlo simulations using the Geant4 toolkit (version 10.06.p03, [21]). We implemented the source spectrum, the three gratings and the detector according to the clinical prototype (see Section III-A). We also included the microscopic structure of the gratings, including auxiliary bridges due to the fabrication process [22]. The incident beam was circular with a diameter of 400 μm, which is slightly smaller than the detector pixel size of 444 μm. The resulting kernel was obtained by recording the energy deposited within the detector by photons that experienced any interaction within the analyzer grating, normalized by the energy deposited by all photons.

The broad active grating area and the lateral fan beam geometry (see Fig. 1A) lead to the beam passing the gratings at angles up to 4.7° with respect to the grating surface normal, and the scanning of the interferometer on a circular arc from −4.7° to 4.7° leads to varying distances between analyzer grating and detector. To obtain a scatter kernel that can be used over the whole field of view, we repeated the scatter kernel simulation with varying incident angle degrees (0° to 4.7° in 10 steps) and varying interferometer positions (0° to 4.7° in 10 steps), obtaining a total of 100 grating scatter kernels. We use the average over all these individual kernels as the resulting kernel for the whole field of view.

D. Sample Scatter

The overall sample scatter intensity depends on sample exposure and of course the sample itself.

Sample scatter is a well-known problem in conventional radiography [23], which is usually counter-acted by placing anti-scatter grids right in front of the detector [24]. In our setup, only a comparably small region of the sample is exposed at once. Additionally, the analyzer grating between sample and detector acts as an anti-scatter grid, which prevents most of the photons scattered at the sample from reaching the detector. We chose not to use an additional anti-scatter grid because of dose considerations. As we found that the amount of sample scatter reaching the detector is significant nevertheless, we need to correct for scatter from the sample.

Both the chemical composition and the spatial distribution of the sample are generally unknown. We adapted the scatter correction software SkyFlow (Philips Medical Systems; [25]), which was originally developed for cases in

conventional radiography where no anti-scatter grid can be used. Patches of the sample are approximated by water spheres featuring a locally identical attenuation signal [26], using the scatter-affected attenuation image. Scatter kernels for different water spheres are calculated beforehand using Monte-Carlo simulations to allow a fast scatter estimation for a sample measurement.

We adapted this approach to dark-field radiography by calculating the respective kernels specifically for the dark-field prototype with its lower tube voltage and increased distance of the patient to the detector compared to conventional radiography. We also included the gratings to account for the anti-scatter grid property of the analyzer grating.

E. Deconvolution

We want to eliminate the influence of crosstalk and scatter from the measurements. For scatter from the sample, this task is performed directly with the adapted SkyFlow software [25], [26]. For scatter from the analyzer grating and detector crosstalk, the respective measured and simulated scattering kernels can be used to perform a deconvolution of measured intensities using the scattering kernel.

Inserting a deconvolution step consistently into the signal retrieval process is not trivial. One basic requirement is that there is no additional noise-dependent bias introduced by the deconvolution step. This rules out just applying Wiener or Maximum Likelihood deconvolution to sample and reference scan separately: both these images feature vastly different noise levels, hence moiré fringes would be dampened by different amounts. For Richardson-Lucy deconvolution, this bias would additionally depend on the location in the image. Therefore, we chose to neglect the influence of noise on the deconvolution step, and resort to deconvolution using the Neumann series. It is explained in the following.

The measured intensity I' is a sum of true model intensity I and scattered intensity I_s:

$$I' = I + I_s = I * (\mathbb{1} + k) =: IK, \quad (18)$$

where the scattered intensity is described by the scattering kernel k (see equation 16), and $\mathbb{1}$ denotes the Kronecker delta. The true intensity I can then be retrieved by performing the inverse

$$I = I'K^{-1}. \quad (19)$$

To approximate the inverse K^{-1}, we use the Neumann series:

$$(1-x)^{-1} = \sum_{n=0}^{\infty} x^n. \quad (20)$$

This leads to

$$I = I' \sum_{n=0}^{\infty} (-k)^{*n} \quad (21)$$

$$= I' - I' * k + I' * k^{*2} - I' * k^{*3} + \dots, \quad (22)$$
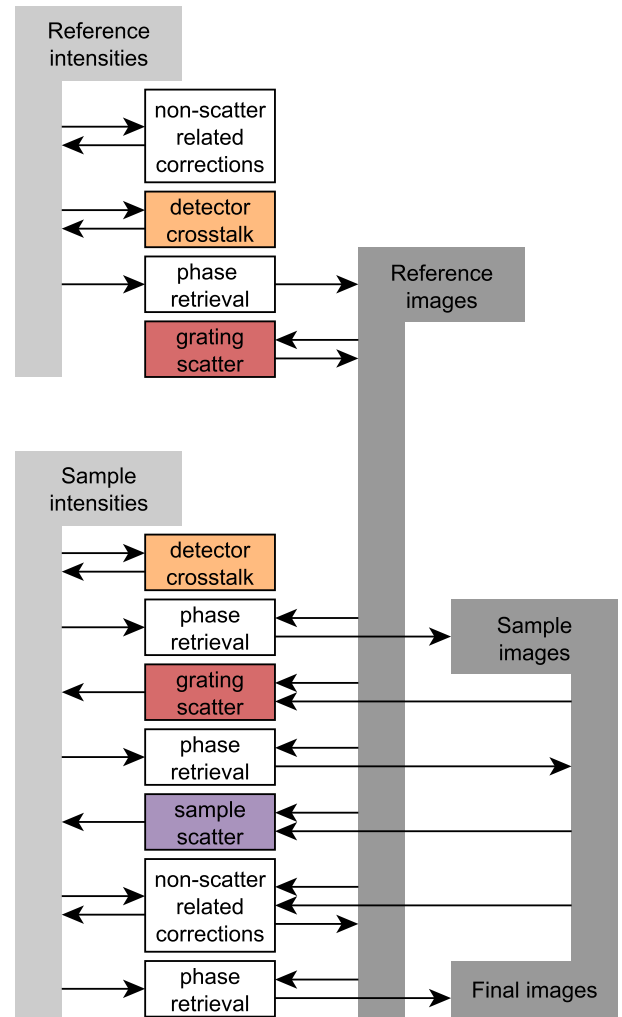
where $*n$ denotes convolving n times.

Fig. 2. Flowchart of processing pipeline. Reference intensities refer to the measured intensities in the reference scans I_j^r, reference images refer to the mean intensity t_j^r, visibility v_j^r, and phase φ_j^r of the fringe pattern without an object, see equation (1). After each consecutive correction of scatter or crosstalk, a phase retrieval with equation (2) is performed on the updated data, whose results are then used to update the data again before the subsequent step.

The Neumann series converges more quickly if the norm of k is small. In order to enhance this, it is beneficial to use a rescaled version

$$\tilde{k} = \frac{\mathbb{1} + k}{|\mathbb{1} + k|} \quad (23)$$

to calculate the approximate inverse. Intuitively, the rescaled operator $\tilde{k}$ is a low-pass filter that preserves the mean of the input signal. Intensities due to crosstalk and scatter from the analyzer grating can then be both positive and negative, depending on whether the measured intensity is higher or lower than in a perfect system without these effects.

F. Image Processing Chain

The overall image processing chain to obtain dark-field and attenuation images from the raw data includes corrections for scatter and crosstalk as well as corrections for other artifacts. The entire processing pipeline is depicted in Fig. 2. Processing is performed from top to bottom of the flowchart.

First, the measured reference intensities are corrected for non-scatter related corrections and detector crosstalk before using equation (1) to calculate the reference images. These are then corrected for scatter from the analyzer grating.

The sample intensities are consecutively corrected for detector crosstalk, scatter from the analyzer grating and scatter from the sample. After each correction, a phase retrieval with equation (2) is performed to update the current sample images before the subsequent step. The final images are obtained from one last phase retrieval after all corrections.

1) Corrections for Scatter: Scatter and crosstalk are corrected for both reference and sample measurements for each exposure separately. For the deconvolution of detector crosstalk, we can directly use the measured intensities as input I' in both reference and sample measurements. For the deconvolution of scatter from the analyzer grating, the intensity distribution reaching the analyzer grating is necessary. In the reference measurement, we use the scatter-affected reference intensity t_j^r as input intensity I' for the deconvolution. In the sample measurement, we use the scatter-affected attenuation image multiplied with the reference intensity t_j^r. In both cases, we then subtract the estimated scattered intensities $I_s = I' - I$ from the measured intensities. Sample scatter is corrected for using the attenuation image and the reference intensity as input for the SkyFlow software [25], [26].

We account for detector saturation by assuming a direct beam in all overexposed pixels. After each correction step, a subsequent phase retrieval is performed to obtain the corrected dark-field and attenuation images.

2) Correction for Mechanical Instabilities: The vibrations of the interferometer arm both during and between exposures in the scanning procedure causes fine fringe-like artifacts in the images. We correct for these vibrations by modelling them in the reconstruction process [15]. The vibration during exposures can only be fitted once scatter is corrected for, as both artifacts lead to a reduced visibility.

3) Correction for Patient Motion: We correct for artifacts induced by motion of the patient, such as unintended breathing or the heartbeat, by locally reducing the number of evaluated exposures and thus the acquisition time for affected pixels [27].

4) Correction for Artifacts Due to Shot Noise: For the effect of falsely increased fitted visibility in areas with low statistic [28], we locally increase the statistic by reducing the image resolution before reconstruction.

5) Correction for Beamhardening-Induced Dark-Field Signal: The spectrum of the X-rays reaching the detector changes between reference and sample measurement, due to spectrally different attenuation in the sample. As the measured visibility also depends on the spectrum, this effect changes the visibility and thus induces a dark-field signal [29], [30]. We correct for this using a look-up table, obtained through calibration measurements with various thicknesses of equivalent absorber material. For the water phantom, we used water as calibration material. For patients, where we do not know the exact tissue composition, we assume that the attenuation is due to soft tissue and bone equally, using water and aluminum as equivalent absorber material.
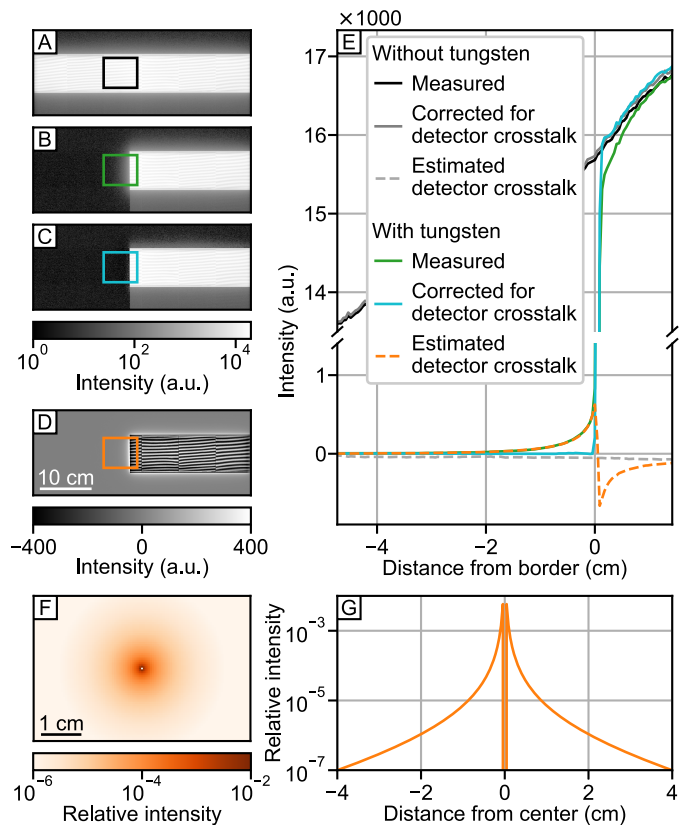

Fig. 3. Measurement and estimation of detector crosstalk. (A), raw detector image without, (B) with the tungsten plate on the detector. (C), detector image in (B) corrected for detector crosstalk (D). (E), profiles of scan with and without the tungsten plates along the indicated rectangles. (F) and (G), the obtained detector crosstalk kernel and its profile.

IV. RESULTS

A. Detector Crosstalk Kernel

To find the kernel parameters, measurements with a 2 mm tungsten plate placed directly in front of the detector, covering about half of it, were conducted. Exemplary raw images without and with the tungsten plate are shown in Fig. 3A and B. Since the tungsten plate absorbs all photons coming directly from the source, the intensity measured behind the tungsten plate is only due to detector crosstalk from the adjacent exposed area.

We performed a least-squares fit for the kernel parameters α and β. The cost function was the difference of the measured intensity behind the tungsten plate to the one estimated from the measured intensity with the current kernel parameters. We used all exposures of one full scan. We found that truncating the Neumann series after five elements (i.e. summation until $n = 4$ in equation (21)) is sufficient, and

$$\alpha = 0.0491 \, \text{mm}^{-1} \; (\sigma_\alpha = 3.33 \times 10^{-6} \, \text{mm}^{-1}) \text{ and}$$
$$\beta = 1.02 \times 10^{-3} \, \text{mm}^2 \; (\sigma_\beta = 0.0489 \times 10^{-6} \, \text{mm}^2).$$

The obtained detector crosstalk kernel k is shown in Fig. 3F and G.

For verification of the crosstalk kernel, we compare the measured crosstalk intensity behind the tungsten plate with the difference between measured and corrected intensity
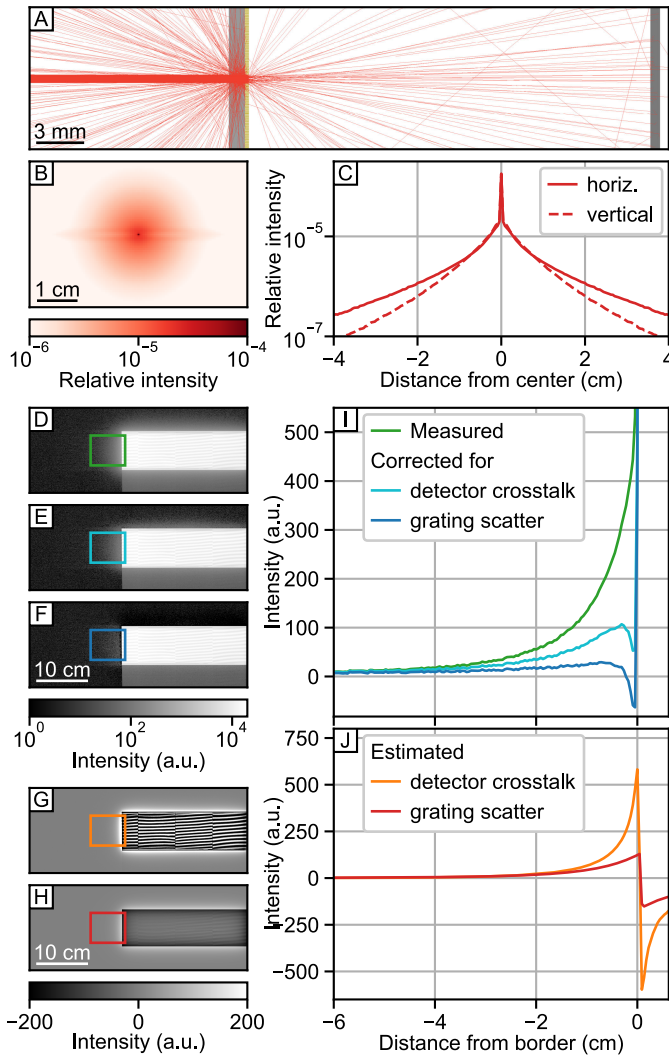
Fig. 4. Simulation and verification of the scatter kernel for the analyzer grating. (A), screenshot of the Monte-Carlo simulation, with paths of photons scattered at the analyzer grating in red. (B), the resulting scatter kernel, with its horizontal and vertical profiles in (C). (D), measurement with the tungsten plate placed upstream of the analyzer grating on the patient contact plane. (E), (F), the intensity corrected for detector crosstalk and scatter from the analyzer grating, with (G) and (H) the respective estimated intensities. (I) and (J), corresponding profiles along the indicated rectangles. After correction for detector crosstalk and scatter from the analyzer grating, the intensity behind the tungsten plate is approximately zero.

$I_s = I' - I$, i.e. the estimated crosstalk intensity for a single exposure (Fig. 3D). The corresponding profiles in Fig. 3E along the indicated rectangles show that the estimated and measured crosstalk intensities behind the tungsten plate agree very well. The corrected intensity has the expected shape with a clear drop at the tungsten border, and is zero behind the tungsten plate.

B. Grating Scatter Kernel

An exemplary screenshot from the Monte-Carlo simulation, showing photons scattered at the analyzer grating, is displayed in Fig. 4A. It illustrates the anti-scatter grid property of the grating, as most forward-scattered photons from the grating substrate are attenuated in the lamellae. The obtained scatter

kernel k is depicted in Fig. 4B. The highly asymmetric shape is due to the horizontal direction of the grating lamellae, allowing a higher fraction of scattered photons travelling in that direction to pass than photons travelling in any other random direction. Therefore, the profile along the horizontal direction is more intense than the vertical one, shown in Fig. 4C.

For verification of the simulated kernel, we conducted again measurements with the 2 mm tungsten plate. However, this time, the plate was placed upstream of the analyzer grating on the patient contact plane. In this configuration, the measured intensity in the plate shadow (Fig. 4D) sums up from scattered photons from the analyzer grating as well as from detector crosstalk. The intensity corrected for detector crosstalk is displayed in Fig. 4E, and the estimated detector crosstalk intensity in Fig. 4G.

The intensity corrected for scatter from the analyzer grating is displayed in Fig. 4F. The estimated scatter from the analyzer grating is shown in Fig. 4H. The corresponding profiles along the indicated rectangles are plotted in Fig. 4I and J. After correction for detector crosstalk and scatter from the analyzer grating, the intensity behind the tungsten plate is approximately zero.

There is a small undershoot close to the tungsten border, which is already present in the profile corrected for detector crosstalk. It is probably due to some inconsistency between the measurement used for fitting the detector crosstalk kernel (Section IV-A) and the one here. However, we would like to point out that this residual artefact is much smaller than the crosstalk effects we are correcting.

C. Sample Scatter

Fig. 5 shows measurements with a water phantom, a cylindrical barrel of 20 cm diameter, at the patient position as an exemplary, well defined sample. A tungsten plate was put between the G_1 and the water phantom in the beam path, such that the water phantom was still fully exposed, but a part of the direct beam was blocked (Fig. 5A). Photons reaching the detector in the shadow of the tungsten plate are due to detector crosstalk, scatter from the analyzer grating, and scatter from the water phantom. The raw images were corrected for detector crosstalk (Fig. 5B and E) and scatter from the analyzer grating (Fig. 5C and F). For the correction of scatter from the water phantom (Fig. 5G), the attenuation image from the same measurement without the tungsten plate was used, as the scatter correction software would otherwise misinterpret the tungsten shadow as high attenuating water. The corresponding profiles of the indicated rectangles are displayed in Fig. 5H and I.

Intensities due to detector crosstalk and scatter from the analyzer grating are higher than sample scatter close to the edge of the tungsten plate, whereas sample scatter is more uniform and has a far higher range. As there is no intensity behind the tungsten plate in the corrected image (Fig. 5D), this shows the validity of the intensity estimation for all three contributions.

An interesting feature is the small step at the tungsten border in the corrected profiles. This is due to the finite focal spot size: As the focal spot has a rectangular shape with peaks at
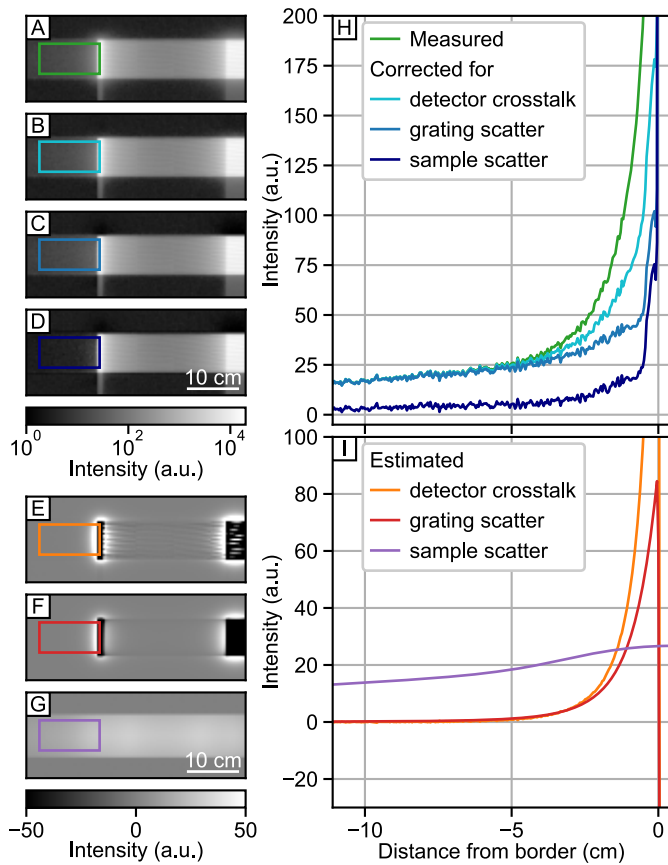
Fig. 5. Verification of sample scatter estimation with a water phantom measurement. (A), measured intensity with a water phantom and the tungsten plate. (B), (C) and (D), the intensity after correction for detector crosstalk, scatter from the analyzer grating, and scatter from the sample, with (E), (F) and (G) the respective estimated intensities. (H) and (I), corresponding profiles along the indicated rectangles for the intensity profiles and scatter and crosstalk intensities. The resulting intensity behind the tungsten plate is flat and close to zero.
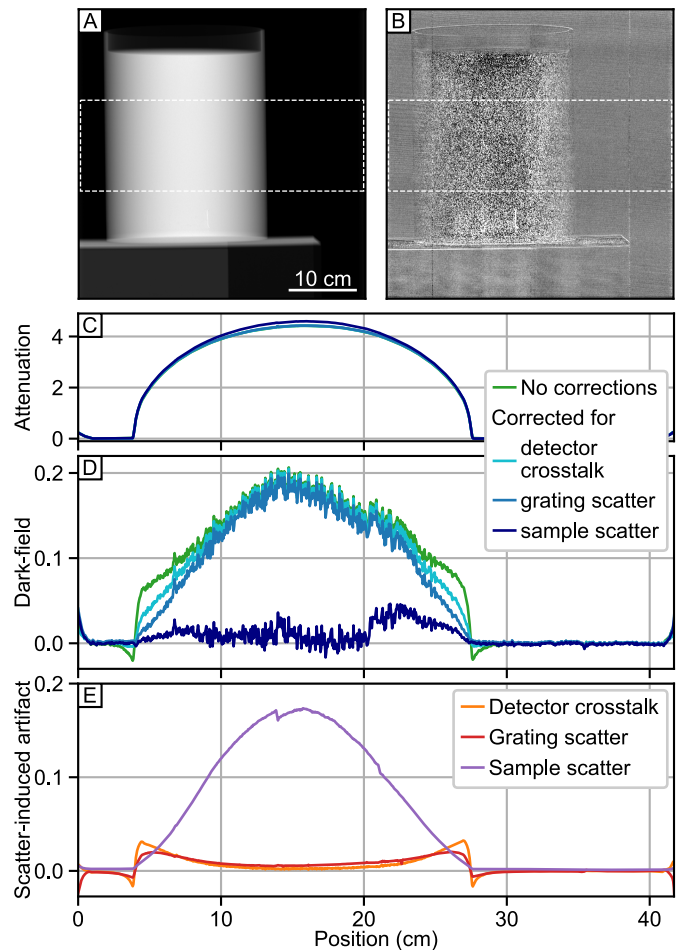

Fig. 6. Validation of corrections with the water phantom. (A), attenuation, and (B), dark-field image after all corrections. (C), and (D), profiles along the indicated rectangles in (A) and (B), after subsequent correction for each contribution. (E), artifacts due to the different contributions. After all corrections, the resulting dark-field signal is zero behind the phantom in most regions, with a small positive remaining artifact on the right.

the edges [31], and the tungsten plate in this measurement is 1.47 m from the source and 0.97 m from the detector, the focal spot width of 1.6 mm leads to this penumbra of 1.1 mm, or 3 pixels, width.

D. Application to Water Phantom Measurement

For a validation of the applied corrections, we imaged the water phantom, described in section III-D. Since water has no micro-structure, the actual dark-field signal is known to be zero everywhere. Fig. 6A and B show the obtained attenuation and dark-field images after all corrections, and Fig 6C, D and E signal profiles after subsequent correction for detector crosstalk, scatter from the analyzer grating and scatter from the sample. The initially measured dark-field signal behind the water phantom is about 0.2. After all corrections, the dark-field signal contains mainly noise.

An interesting detail is the small undershoot just outside the water phantom if no correction is applied (Fig. 6D). It is created by a reduced blur of the interference pattern in the sample scan compared to the reference scan, due to less crosstalk from the neighboring pixels behind the object.

The kinks visible in the sample scatter artifact in Fig 6E are located at the borders between grating tiles. As the tiles

attenuate slightly differently, the primary intensity reaching the detector varies per grating tile, while the sample scatter estimation does not include tile-wise information.

Similarly, the small remaining artifact up to about 0.05 on the right and the smaller one of up to 0.02 in the center (Fig. 6D) are most likely due to the grating tile having slightly different structure or alignment, as the edges of these artifacts correspond to borders between grating tiles.

E. Application to Patient Images

Fig. 7 and Fig. 8 show chest images of an 42-year old woman imaged in posterior-anterior and lateral orientation, respectively. All images are corrected for non-scatter related effects as described in Section III-F. The respective images in the top row (B), (C), and (D) are reconstucted with either one of the presented corrections disabled. The respective correction's effect can additionally be seen from the difference of the dark-field images to the one reconstructed with all corrections, shown in the respective panels (F), (G), and (H).

If either one of the corrections is disabled, there is an additional, spurious signal in addition to the true dark-field signal of the lung. Detector crosstalk and scatter from the
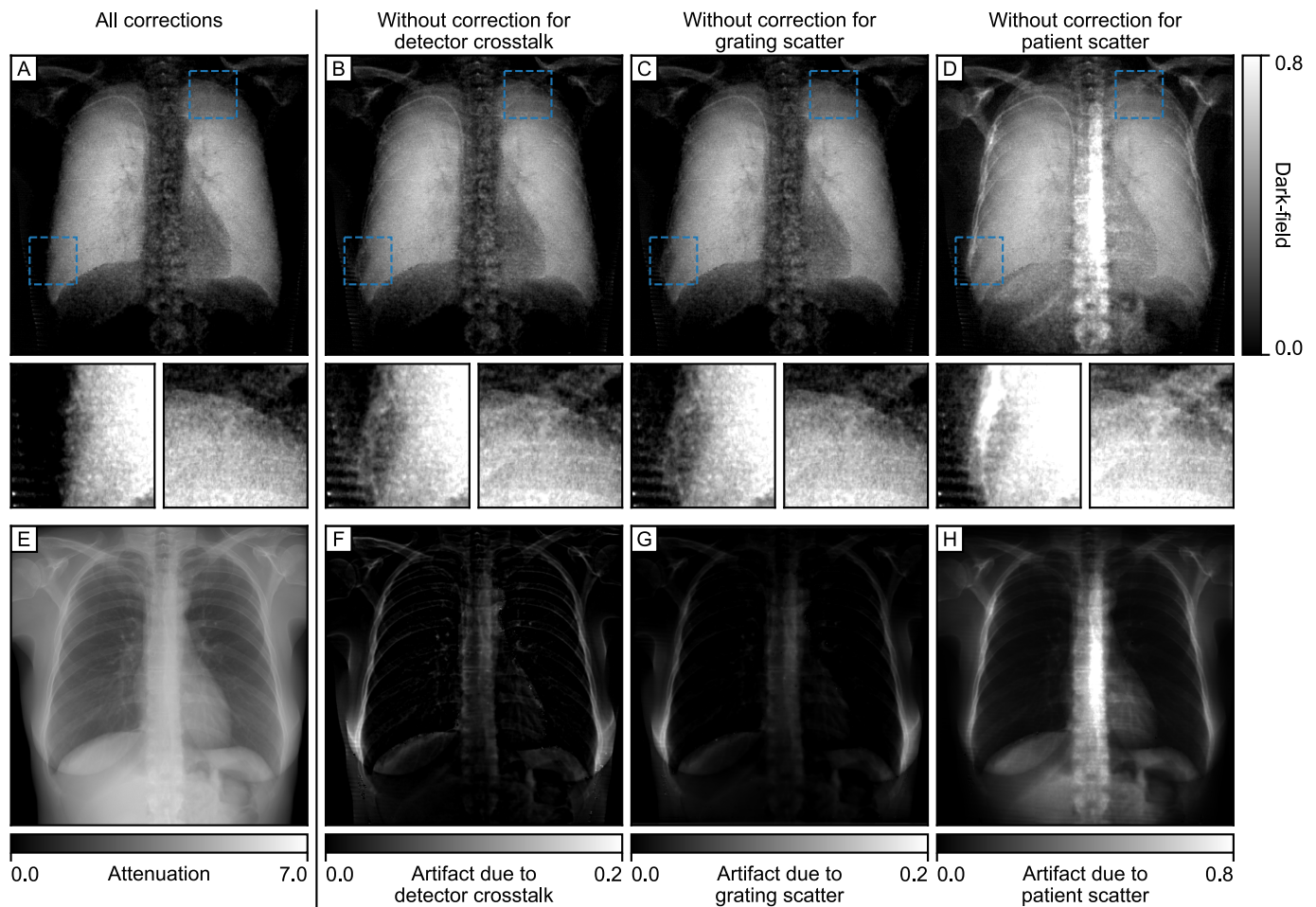
Fig. 7. The effect of correcting scatter and crosstalk in dark-field chest radiographs of a 42-year old woman imaged in posterior-anterior orientation. (A), with all the presented corrections for scatter and crosstalk. (B), without correction for detector crosstalk. (C), without correction for scatter from the analyzer grating. (D), without correction for scatter from the patient. (E), attenuation image, corrected for scatter and crosstalk, without the contrast enhancement normally applied before diagnostic evaluation. (F), artifact due to detector crosstalk. (G), artifact due to scatter from the analyzer grating. (H), artifact due to scatter from the patient. The different contributions cause different artifacts in the dark-field image, which can be removed with the corrections.

analyzer grating have their strongest impact in the vicinity of edges in the attenuation image, such as the clavicle in the shoulder region in the posterior-anterior image, the region around the sternum in the lateral images, and the rib cage close to the direct beam (see zoom-ins). Due to the larger regions with direct beam, the influence of detector crosstalk and scatter from the analyzer grating is larger in lateral than in posterior-anterior orientation.

The scatter from the patient itself mainly affects regions where the overall attenuation is highest, such as the abdomen and spine in the posterior-anterior images and the abdomen and shoulders in the lateral images.

These artifacts impede the qualitative assessment of the dark-field signal of the lung, as e.g. the lower edges of the recessus behind the diaphragm cannot clearly be distinguished without a correction for sample scatter. Furthermore, these artifacts make a quantitative assessment impossible. With all corrections, the previously described artifacts are eliminated.

V. DISCUSSION

We describe the influence of scatter and crosstalk on dark-field radiographs, and propose methods to find the respective scattering kernels, enabling a deconvolution-based correction of the induced artifacts. The overall influence of scatter and crosstalk in dark-field images is substantial. Especially in regions with high attenuation such as the abdomen and spine, there is a high ratio of scatter to primary intensities, and the apparent dark-field signal is actually dominated by artifacts.

The proposed algorithms correct separately for the three main contributions detector crosstalk, scatter from the analyzer grating, and scatter from the sample. We used different methods to obtain the respective kernels due to the different mechanisms. Measurements where the primary beam is partially blocked are used to show that the estimated intensities match the measured ones for all three contributions. With a water phantom we validate the correction of the dark-field images quantitatively.

The water phantom is a very simple sample, whose material and spatial distribution can be very well modelled by the scatter correction software for sample scatter. In a real patient, there are other materials present which may be distributed quite differently along the beam path, so the approximation with water spheres might lead to less realistic sample scatter corrections.
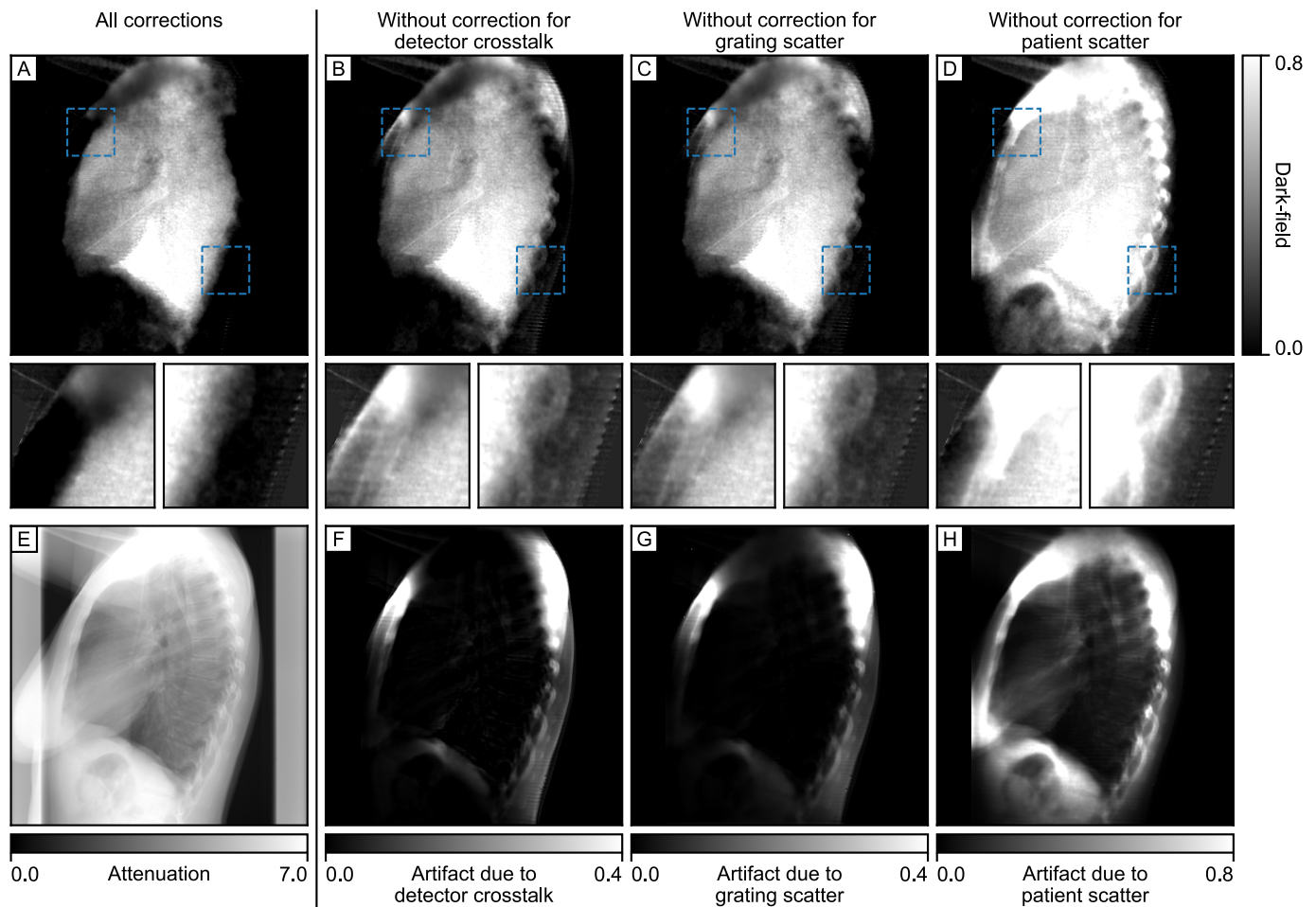
Fig. 8. Dark-field radiographs with corrections for scatter and crosstalk of the same woman as in Fig. 7, imaged in lateral orientation. (A), with all the presented corrections for scatter and crosstalk. (B), without correction for detector crosstalk. (C), without correction for scatter from the analyzer grating. (D), without correction for scatter from the patient. (E), attenuation image, corrected for scatter and crosstalk, without the contrast enhancement normally applied before diagnostic evaluation. (F), artifact due to detector crosstalk. (G), artifact due to scatter from the analyzer grating. (H), artifact due to scatter from the patient.

Another potential source of incorrect scatter or crosstalk correction is detector saturation. As we use raw images for the correction of detector crosstalk and attenuation images for the correction of scatter from the analyzer grating and the sample, wrong values in these images also cause wrong corrections. A first counter-measure is a careful collimation to minimize the detector area not covered by the patient. Further, we reduce the effect of detector saturation by assuming a direct beam in all overexposed pixels. However, this assumption is not correct everywhere, as image areas might still run into detector saturation despite low attenuating sample features.

For sample scatter, there are other methods to reduce its influence in chest radiography. One method is to target the overall amount of scatter generated, by exposure of a smaller portion of the sample at a time [32]. For clinical dark-field radiography, a further reduction of the active grating area and thus the exposed region is not feasible, as this would result in overall longer image acquisition times, meaning the patient would have to stand still and hold breath even longer. Another method would be to prevent the scattered photons from reaching the detector by the use of anti-scatter grids. This would further reduce the dose-efficiency of this method.

Both these methods can only reduce the influence of sample scatter and not eliminate it [33] and [34], in contrast to a software-based correction.

There are also other processes that influence the measured visibility and corrupt the quantitative dark-field signal, as described in Section III-F. The residual dark-field signal near the clavicle in the lateral image indicates that at least one of all the applied corrections is not entirely correct, since there are no corresponding areas of strong dark-field signal in the posterior-anterior image. The high attenuation in this area leads to very little primary intensity, making this area very sensitive to correct scatter and crosstalk estimates. The scatter and crosstalk corrections however are impeded by a relatively large amount of bone in the beam path and the close proximity of a direct beam causing detector saturation.

The patient images show that the overall influence of scatter from the sample is much larger than the one from detector crosstalk and scatter from the analyzer grating. This is because the whole exposed sample region acts as a source of scattered photons, with a high spatial range across the whole detector, whereas the range of detector crosstalk and scatter from the analyzer grating is much smaller.

The exact scatter and detector crosstalk kernels used in this work depend on the used setup, as e.g. the anti-scatter grid properties of the analyzer grating depend on the grating parameters, and overall scatter reaching the detector depends on the beam spectrum and the distances. This means that all measurements and simulations to obtain these kernels will have to be repeated whenever the setup is changed. For a hypothetical future setup featuring gratings that cover the whole field of view, the overall exposed area on the sample will increase, leading to even more scatter from the sample. This will require further investigation. However, the general concepts behind the corrections presented here are applicable for all grating-based radiography systems, including even the recently presented clinical dark-field CT system [35].

CONCLUSION

With the corrections presented here – and other non-scatter related corrections – the obtained dark-field signal is due to the micro-structure of the tissue, and differences between the dark-field signal of different patients can be attributed to their lung condition rather than scatter or crosstalk artifacts. This ensures a unobstructed qualitative evaluation, and enables a quantitative evaluation of dark-field radiographs.

REFERENCES

[1] F. Pfeiffer et al., "Hard-X-ray dark-field imaging using a grating interferometer," *Nature Mater.*, vol. 7, no. 2, pp. 134–137, Feb. 2008.

[2] A. Momose, "X-ray phase imaging reaching clinical uses," *Phys. Medica*, vol. 79, pp. 93–102, Nov. 2020.

[3] K. Willer et al., "X-ray dark-field chest imaging for detection and quantification of emphysema in patients with chronic obstructive pulmonary disease: A diagnostic accuracy study," *Lancet Digit. Health*, vol. 3, no. 11, pp. e733–e744, Nov. 2021.

[4] T. Urban et al., "Qualitative and quantitative assessment of emphysema using dark-field chest radiography," *Radiology*, vol. 303, no. 1, pp. 119–127, Apr. 2022.

[5] M. Frank et al., "Dark-field chest X-ray imaging for the assessment of COVID-19-pneumonia," *Commun. Med.*, vol. 2, no. 1, p. 147, Nov. 2022.

[6] F. T. Gassert et al., "X-ray dark-field chest imaging: Qualitative and quantitative results in healthy humans," *Radiology*, vol. 301, no. 2, pp. 389–395, Nov. 2021.

[7] W. Yashiro, Y. Terui, K. Kawabata, and A. Momose, "On the origin of visibility contrast in X-ray Talbot interferometry," *Opt. Exp.*, vol. 18, no. 16, p. 16890, 2010.

[8] J. Graetz, A. Balles, R. Hanke, and S. Zabler, "Review and experimental verification of X-ray dark-field signal interpretations with respect to quantitative isotropic and anisotropic dark-field computed tomography," *Phys. Med. Biol.*, vol. 65, no. 23, Nov. 2020, Art. no. 235017.

[9] Z.-T. Wang, K.-J. Kang, Z.-F. Huang, and Z.-Q. Chen, "Quantitative grating-based X-ray dark-field computed tomography," *Appl. Phys. Lett.*, vol. 95, no. 9, Aug. 2009, Art. no. 094105.

[10] F. Pfeiffer, T. Weitkamp, O. Bunk, and C. David, "Phase retrieval and differential phase-contrast imaging with low-brilliance X-ray sources," *Nature Phys.*, vol. 2, pp. 258–261, Apr. 2006.

[11] A. Momose, S. Kawamoto, I. Koyama, Y. Hamaishi, K. Takai, and Y. Suzuki, "Demonstration of X-ray Talbot interferometry," *Jpn. J. Appl. Phys.*, vol. 42, pp. L866–L868, Jul. 2003.

[12] O. Glatter and O. Kratky, *Small Angle X-Ray Scattering*. New York, NY, USA: Academic, 1982.

[13] S. Vedantham, L. Shi, and A. Karellas, "Large-angle X-ray scatter in Talbot–Lau interferometry for breast imaging," *Phys. Med. Biol.*, vol. 59, no. 21, pp. 6387–6400, Oct. 2014.

[14] J. Vignero, S. Rodríguez-Pérez, N. Marshall, and H. Bosmans, "Minimizing the scatter contribution and spatial spread due to the absorption grating G2 in grating-based phase-contrast imaging," *Proc. SPIE*, vol. 10573, pp. 1146–1152, Mar. 2018.

[15] W. Noichl et al., "Correction for mechanical inaccuracies in a scanning Talbot-Lau interferometer," *IEEE Trans. Med. Imag.*, vol. 43, no. 1, pp. 28–38, Jan. 2024.

[16] V. Revol et al., "X-ray interferometer with bent gratings: Towards larger fields of view," *Nucl. Instrum. Methods Phys. Res. A, Accel. Spectrom. Detect. Assoc. Equip.*, vol. 648, pp. S302–S305, Aug. 2011.

[17] C. Kottler, F. Pfeiffer, O. Bunk, C. Grünzweig, and C. David, "Grating interferometer based scanning setup for hard X-ray phase contrast imaging," *Rev. Sci. Instrum.*, vol. 78, no. 4, Apr. 2007, Art. no. 043710.

[18] T. Koehler et al., "Slit-scanning differential X-ray phase-contrast mammography: Proof-of-concept experimental studies," *Med. Phys.*, vol. 42, no. 4, pp. 1959–1965, 2015.

[19] W. Zhao, G. Ristic, and J. A. Rowlands, "X-ray imaging performance of structured cesium iodide scintillators," *Med. Phys.*, vol. 31, no. 9, pp. 2594–2605, Sep. 2004.

[20] V. N. Hansen, W. Swindell, and P. M. Evans, "Extraction of primary signal from EPIDs using only forward convolution," *Med. Phys.*, vol. 24, no. 9, pp. 1477–1484, Sep. 1997.

[21] S. Agostinelli et al., "GEANT4—A simulation toolkit," *Nucl. Instrum. Methods Phys. Res. A, Accel. Spectrom. Detect. Assoc. Equip.*, vol. 506, no. 3, pp. 250–303, 2003.

[22] J. Mohr et al., "High aspect ratio gratings for X-ray phase contrast imaging," *AIP Conf. Proc.*, vol. 1466, no. 1, pp. 41–50, 2012.

[23] H. P. McAdams, E. Samei, J. Dobbins, G. D. Tourassi, and C. E. Ravin, "Recent advances in chest radiography," *Radiology*, vol. 241, no. 3, pp. 663–683, Dec. 2006.

[24] G. T. Barnes, "Contrast and scatter in X-ray imaging," *RadioGraphics*, vol. 11, no. 2, pp. 307–323, Mar. 1991.

[25] D. Mentrup, S. Jockel, B. Menser, and U. Neitzel, "Iterative scatter correction for grid-less bedside chest radiography: Performance for a chest phantom," *Radiat. Protection Dosimetry*, vol. 169, nos. 1–4, pp. 308–312, Jun. 2016.

[26] M. Bertram, S. Hohmann, and J. Wiegert, "SU-FF-I-22: Scatter correction for flat detector cone-beam CT based on simulated sphere models," *Med. Phys.*, vol. 34, pp. 2342–2343, Jun. 2007.

[27] R. C. Schick et al., "Correction of motion artifacts in dark-field radiography of the human chest," *IEEE Trans. Med. Imag.*, vol. 41, no. 4, pp. 895–902, Apr. 2022.

[28] M. Chabior, T. Donath, C. David, M. Schuster, C. Schroer, and F. Pfeiffer, "Signal-to-noise ratio in X ray dark-field imaging using a grating interferometer," *J. Appl. Phys.*, vol. 110, no. 5, Sep. 2011, Art. no. 053105.

[29] G. Pelzer et al., "A beam hardening and dispersion correction for X-ray dark-field radiography," *Med. Phys.*, vol. 43, pp. 2774–2779, Jun. 2016.

[30] F. De Marco et al., "X-ray dark-field signal reduction due to hardening of the visibility spectrum," *IEEE Trans. Med. Imag.*, early access, Nov. 30, 2024, doi: 10.1109/TMI.2023.3337994.

[31] R. Behling, *Modern Diagnostic X-Ray Sources: Technology, Manufacturing, Reliability*. Boca Raton, FL, USA: CRC Press, 2021.

[32] E. Samei et al., "Comparative scatter and dose performance of slot-scan and full-field digital chest radiography systems," *Radiology*, vol. 235, no. 3, pp. 940–949, Jun. 2005.

[33] L. T. Niklason, J. A. Sorenson, and J. A. Nelson, "Scattered radiation in chest radiography," *Med. Phys.*, vol. 8, no. 5, pp. 677–681, Sep. 1981.

[34] C. E. Floyd, J. A. Baker, J. Y. Lo, and C. E. Ravin, "Measurement of scatter fractions in clinical bedside radiography," *Radiology*, vol. 183, no. 3, pp. 857–861, Jun. 1992.

[35] M. Viermetz et al., "Dark-field computed tomography reaches the human scale," *Proc. Nat. Acad. Sci. USA*, vol. 119, no. 8, Feb. 2022, Art. no. e2118799119.